

Metal Halide Perovskites Demonstrate Radiation Hardness and Defect Healing in Vacuum

Michael Holland, Anthony Ruth, Kamil Mielczarek, Vivek V. Dhas, Joseph J. Berry, and Michael D. Irwin*

Cite This: <https://doi.org/10.1021/acsami.1c24709>

Read Online

ACCESS |

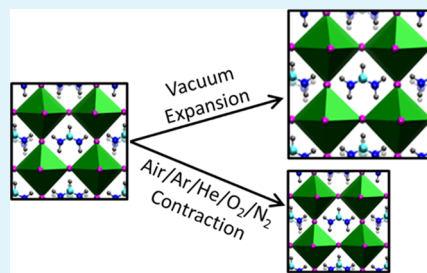
Metrics & More

Article Recommendations

Supporting Information

ABSTRACT: Herein, we subject formamidinium lead iodide films to oxygen-containing gases (flowing O₂ or free diffusion of lab atmosphere), inert gases (flowing He, Ar, or N₂), and vacuum. Our films are irradiated by Cu K α X-rays and held at 75 °C while X-ray diffraction is recorded. Under all gas conditions, we observe a reproducible $1.1 \pm 0.5 \text{ \AA}^3$ perovskite lattice contraction from an initial unit cell volume of $256.5 \pm 0.8 \text{ \AA}^3$ concurrent with continuous perovskite loss and lead iodide growth. Oxygen-containing gases increase the reaction rates without materially altering perovskite structural changes. Under the same temperature and irradiation conditions *in vacuo*, a self-healing reaction is observed, exhibited by a reproducible ($0.9 \pm 0.3 \text{ \AA}^3$) lattice expansion and stabilization of the perovskite. Interactions between the perovskite, defects, and minority phases are simulated by generalized gradient approximation Perdew–Burke–Ernzerhof (GGA-PBE) density functional theory. Lattice contraction indicates an increase in the concentration of Schottky defects—pairs of formamidinium and iodine vacancies. Under irradiation in every atmospheric condition, a solid solution of Schottky defects with a concentration of several percent diffuses and precipitates forming lead iodide and consuming the defects. In the presence of ionized gases, this framework is modified to include the continual loss of formamidinium and iodine ions from the perovskite forming Schottky defects.

KEYWORDS: perovskites, photovoltaics, *in vacuo*, Schottky defects, environmental degradation, X-ray diffraction, ion migration



INTRODUCTION

Metal halide perovskites (MHPs) have become an important focus of intensive research for potential applications in devices including solar cells, light-emitting diodes, lasers, and X-ray photodetectors.^{1,2} A persistent challenge to commercialization of MHP-based optoelectronic devices is ensuring long-term stability under operating conditions.³ Understanding the processes that degrade MHP thin films is essential for extending operational device lifetimes. In contrast, MHP devices have demonstrated enhanced stability under ionizing radiation compared to alternative photovoltaic absorber materials and are candidate space-based solar applications.⁴ Bare MHP films in vacuum conditions degrade under electron beam irradiation but resist damage from proton beams, while under atmospheric conditions, proton beam irradiation causes degradation forming PbO.⁵

Common MHP thin film fabrication methods are expected to generate elevated crystallographic point defect concentrations when compared to single-crystal samples.⁶ MHP crystals are stabilized against high concentrations of such defects through redistribution mediated by ion migration.⁷ While the reduction of device performance is a degradation indicator, it is not always clear where or how the degradation occurs, whether in the bulk of the perovskite layer, at the interfaces between the perovskite and an adjacent layer, or in another layer of the device stack. We avoid such ambiguity

here by examining degradation processes that directly alter the perovskite layer.

In this study, we focus specifically on an examination of defects and degradation of solution-processed mixed cation formamidinium/cesium lead iodide perovskite (FA_{1-x}Cs_xPbI₃; $x < 0.05$). Similar samples were characterized by XPS as reported previously, finding a near-stoichiometric ABX₃ surface composition.⁸ By monitoring MHP thin films using continuous X-ray diffraction, we see how interactions with ionized gases change defect generation at the perovskite surface through associated changes to the perovskite bulk. MHP thin films are bombarded by ionizing X-rays at elevated temperature to stress and degrade the MHP thin films. The thin films are monitored over 50 h long test cycles where 49 diffraction patterns are collected. To probe the role of the atmosphere in perovskite structural degradation under these conditions, our study includes tests performed under a variety of flowing gases (N₂, He, O₂, and Ar), under diffusion of laboratory atmosphere, and under vacuum.^{9,10}

Received: December 21, 2021

Accepted: January 27, 2022

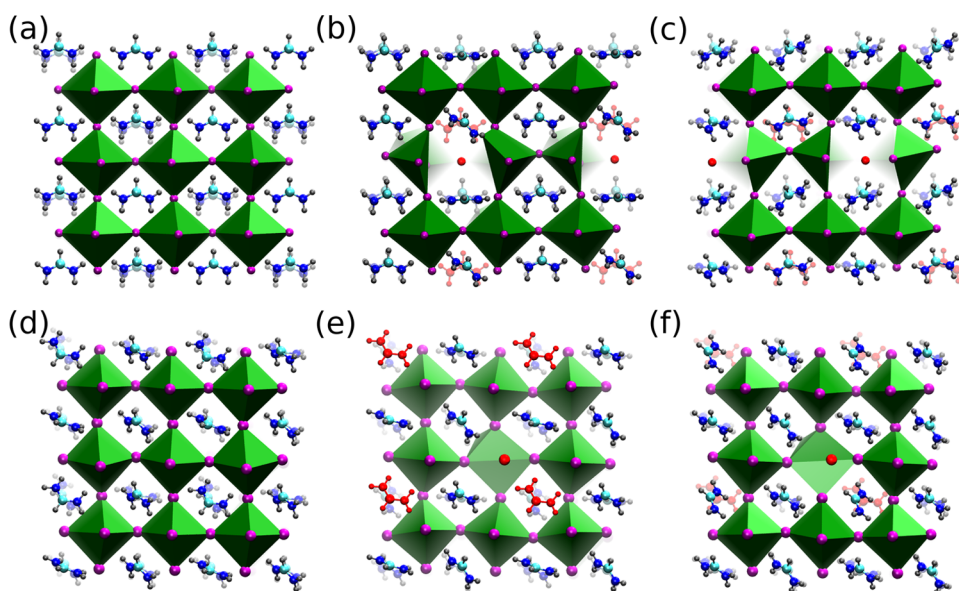


Figure 1. Atomistic representations of FAPbI₃. All periodic supercells are 2 × 2 × 2, 3 × 3 octahedra grids and 4 × 4 FA grids are shown for clarity. Depth cueing is used to indicate foreground and background species. Vacancies are denoted by red ball-and-stick structures in the ion's original location. (a–c) Monomorphic structures and (d–f) polymorphic structures. Panels (a) and (d) are stoichiometric perovskite. Panels (b) and (e) have an FA and I vacancy at a distance of $a\frac{\sqrt{2}}{2}$, where a is the lattice parameter. Panels (c) and (f) have an FA and I vacancy at a distance of $a\frac{\sqrt{5}}{2}$.

Significant changes in X-ray-driven perovskite degradation kinetics and lattice structures are observed when the sample chamber is under vacuum as compared to degradation under any of the gases investigated. Oxygen-containing atmospheres affect the fastest degradation of the perovskite followed by argon, then nitrogen, and finally helium.

Total diffracted peak intensities of perovskite (I_{FAPbI_3}) and PbI₂ (I_{PbI_2}) and experimentally measured unit cell volume (V_{exp}) are monitored throughout degradation test cycles. Changes to the perovskite diffraction patterns indicate lattice contraction in all test conditions except vacuum. It is noteworthy that defect generation is commensurate with the net loss of perovskite material; $\Delta I_{\text{FAPbI}_3}$ likely involves reactions at surfaces/grain boundaries, while changes to the unit cell volume, ΔV_{exp} , as measured by XRD necessarily require changes to the perovskite bulk.

RESULTS AND DISCUSSION

Lead iodide is the only degradation product observed directly by diffraction, but there are modes of perovskite degradation that do not produce significant changes to lead iodide signal intensity—especially but not exclusively in the presence of oxygen—indicating the production of at least one unidentified lead-containing degradation product. The results are also consistent with a process where Schottky defects (cation and anion vacancies occurring in charge-balancing ratios) are generated at the surface of the perovskite by interactions with gases in the sample chamber, diffuse into the bulk of the perovskite causing the crystal lattice to contract, and interact with perovskite decomposition products present as minority phases in the films. Relationships between vacancy concentrations and unit cell volume have been investigated computationally in perovskites and experimentally in other materials.^{5,6} We present estimated changes in Schottky vacancy concentration (y in (FAI)_{1-y}PbI₂) in these experiments based on *ab initio* calculations. The chemistry and crystal structure

observed herein are rationalized by first-principles density functional theory (DFT) calculations. Notably, Schottky defects were considered using both monomorphic and polymorphic representations (Figure 1) following the nomenclature of Dalpian et al.³⁹

We rationalize $\Delta I_{\text{FAPbI}_3}$ and ΔV_{exp} as resulting from a series of processes occurring within the atmosphere, at the perovskite surface, and in the perovskite bulk.

We observe an accelerating influence of ionizing radiation on perovskite degradation. Nominally inert gases become reactive in the presence of ionizing radiation. The effects on perovskite loss rate (k_{FAPbI_3}) and PbI₂ growth rate (k_{PbI_2}) are evaluated from the standpoint of chemical kinetics. Degradation rates do not track well with the ionization energy of the gas used and thus are not limited by the rate of direct X-ray ionization of the gas.

Defect-mediated phenomena in perovskites such as giant photoconductivity and photocapacitance, the light soaking effect, and degradation under active conditions appear to require stimuli to trigger defect-related ionic mobility.^{6,11–14} Central to the question of ionic mobility is interactions between oppositely charged defects and their ability to bind or agglomerate. Defect concentrations were estimated from ΔV_{exp} by calculating the change in volume from DFT calculations (ΔV_{DFT}) at known defect concentrations.

Ion mobility in MHPs has been well established and identified as playing an important role in the degradation of the perovskite.^{6,11,12,14–33} Migration of A-site and X-site ions out of the perovskite layer and into adjacent layers has been observed in devices, and X-site ion migration plays a central role in the known phase segregation effects observed in mixed halide perovskites.^{26,34} “Champion” devices have been observed to show greater resistance to the degradation caused by ion migration than poorer-performing samples from the same studies.^{22,31} Improving perovskite stability by limiting ion migration is reasonably expected to improve the associated optoelectronic performance of MHP-based devices. Targets for

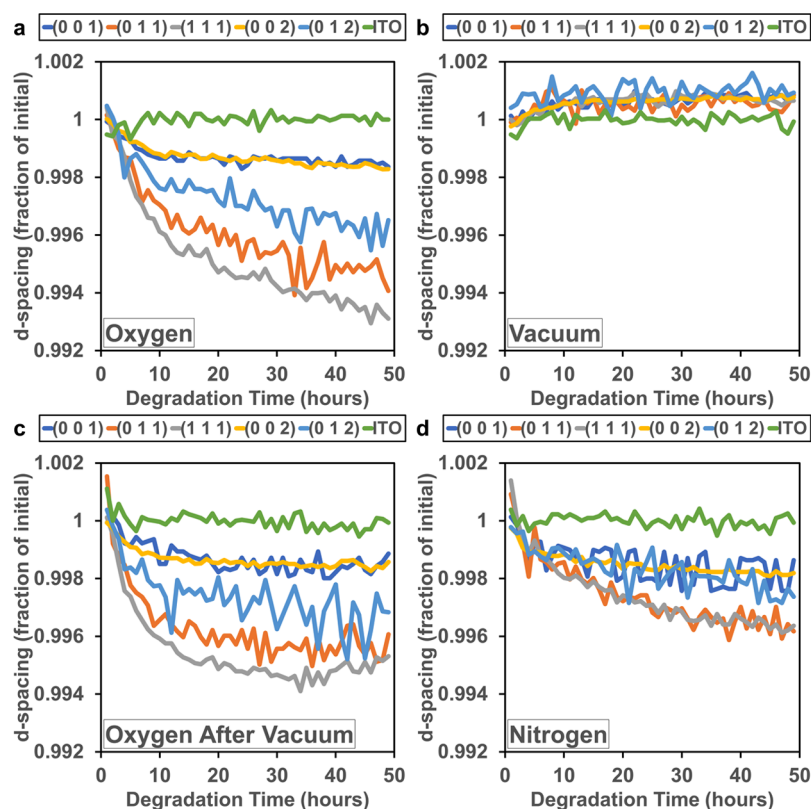


Figure 2. Fractional changes to reflection *d*-spacings. Each perovskite XRD peak normalized to its expected *d*-spacing from the initial measured unit cell over the course of (a) an O₂ flow test, (b) a vacuum test, (c) an O₂ flow test performed after and on the same sample as the vacuum test, and (d) a N₂ flow test. Fractional changes to the ITO peak (green lines) are included as an internal standard.

decreasing ion migration rates include minimizing defect concentrations and limiting ion diffusion through adjacent device layers. In this work, we uncover a mechanism for the reduction of Schottky defect concentrations in thin films of formamidinium lead iodide perovskite.

Sequential X-ray diffraction measurements were used to monitor changes in thin films of FAPbI₃ perovskite held at a temperature of 75 °C and continuously irradiated with 8.04 keV X-rays under controlled-environment conditions. Experiments were performed with a heated, enclosed sample stage. Results are compared for flowing gases (He, N₂, O₂, and Ar), open diffusion of laboratory atmosphere through the stage, and continuous evacuation. Degradation of the perovskite films in this study is evaluated by three metrics: perovskite diffraction intensity (*I*_{FAPbI₃}), lead iodide diffraction intensity (*I*_{PbI₂}), and perovskite unit cell volume (*V*_{exp}), and their changes between measurements.

*V*_{exp} changes under all test conditions. In all tests under atmosphere or flowing gas, the lattice is observed to contract; however, in all vacuum tests, the lattice expands (Figure 2).

The extent of lattice contraction was indistinguishable between oxygen and inert gases. In addition to *V*_{exp} changes, some of our tests showed shifts in the ratios of reflection *d*-spacings that indicate that the perovskite lattice undergoes a symmetry breaking (possibly rhombohedral) out-of-cubic distortion (Figure 2). The distortions are small (corresponding to a rhombohedral angle less than 0.5° off cubic) but real, being well within the resolution of the measurement. In the final XRD pattern from one of the oxygen flow tests, the (111) reflection is observed at a 2θ angle of 24.3801°, 0.1304° higher than expected for a cubic lattice based on the (001) *d*-

spacing in the same pattern. Within the precision of our measurements, initial diffraction patterns do not show the out-of-cubic distortion and there is also no distortion observed under vacuum testing. Full trajectories showing the fractional changes in *d*-spacing of five perovskite reflections (001), (011), (111), (002), and (012) for all tested samples are available in the Supporting Information.

A comparison of peak shifting to peak broadening (Figure 3) highlights the fact that changes to peak width are smaller and occur at a different time than changes to peak *d*-spacings. Peaks broaden when the distribution of the distances between lattice planes increases, and shift when the average distance between lattice planes changes. In Figure 3, peaks shift throughout the test, while broadening reaches a steady condition after the first few scans. We attribute the peak broadening to the establishment of vacancy defect concentration gradient within the perovskite domains and the shifting to the increasing total defect concentration.

One possible explanation for the perovskite lattice contraction under gas, but not under vacuum, would be the action of volatile components (solvents) leftover from the perovskite fabrication. Under vacuum, these volatile components might be removed, leaving a stable material. To evaluate this “solvent hypothesis”, a sample (V-C) was first tested under vacuum conditions and then tested a second time under a flowing oxygen (Figure 2b,c). This is compared to a control sample (V-A) tested only under a flowing oxygen (Figure 2a). Under vacuum, the tested sample shows the characteristic lattice expansion seen in other vacuum tests and no out-of-cubic distortion. Both the postvacuum oxygen test and the control oxygen test show the characteristic lattice contraction

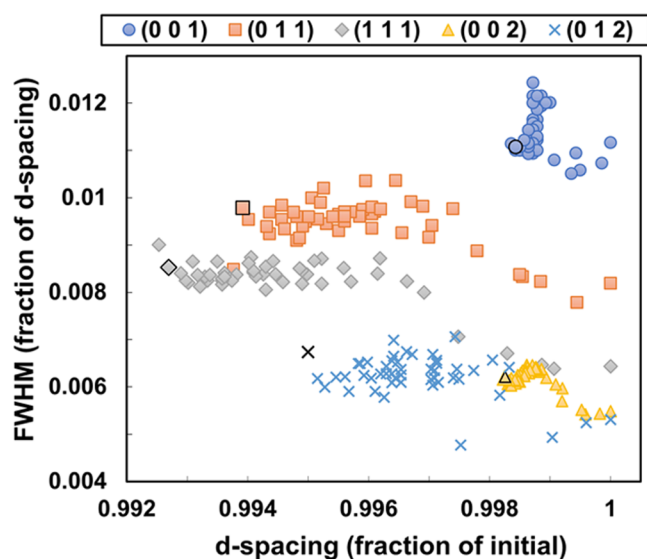


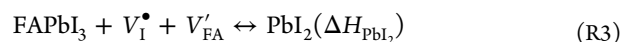
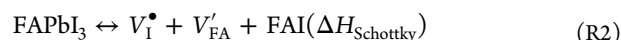
Figure 3. Changes in perovskite *d*-spacings vs FWHM for sample V-A (oxygen flow test). A comparison of fractional changes in peak *d*-spacings with changes in the peak full width at half-maximum over the course of an O₂ flow test shows that peak shifting continues after peak broadening has stabilized. The outlined data point in each series indicates the last value measured.

along with the out-of-cubic distortion. Loss of perovskite diffraction signal was negligible in the vacuum test but significant in both oxygen flow tests. These results disqualify the “solvent hypothesis” explanation of the lattice changes, as residual solvent should either be removed under vacuum or produce the same effects in the vacuum test and the gas flow tests. Interestingly, the lattice contracted by approximately the same absolute amount in both the vacuum first sample and the control, even though the vacuum first sample underwent a lattice expansion during the vacuum test.

A test to look for lattice expansion under vacuum following an initial lattice contraction under gas was performed. Sample IV-C was first tested under a flowing argon gas, exhibiting lattice contraction, and then a second test cycle under vacuum was performed and lattice expansion was seen; this is illustrated in the Supporting Information (Figure S4). Partial lattice re-expansion between the test under argon and the subsequent vacuum test is observed, while in sample V-C, the lattice expansion under vacuum was fully retained at the beginning of the subsequent oxygen test.

Representation of MHPs has proven to be a unique challenge for density functional theory. In the cubic α -phase structure at room temperature, FA cations are presumed to rotate in place.³⁵ However, others report that FA rotational modes begin to freeze-out slightly below room temperature resulting in a cubic-to-tetragonal phase transition and may be significantly affected by lattice contraction or expansion.^{36,37} The FA⁺ dipole moment prefers orienting along the (100) and (111) directions.³⁵ DFT, 0 K structures necessarily have each FA cation in a fixed orientation. Monomorphic representations of FAPbI₃ align every FA molecule along the (100) direction, which can be done with a single unit cell.³⁸ Relaxation results in an orthorhombic structure with lattice parameters ordered by the FA⁺ molecule’s dimensions. Polymorphic supercells, which start with a random orientation of each organic cation, result in nearly cubic lattice parameters and electronic structure. Polymorphic supercells have demonstrated accurate

GGA-PBE band gaps of alloyed perovskites.^{6,16,24,34,39–47} Reaction enthalpy differences between monomorphic and polymorphic calculations rationalize differences in defect formation energies reported by various authors on the basis of structural representation. Furthermore, structural reorientation following defect formation is different in the monomorphic and polymorphic cases, highlighting the interactions between the defect and the surrounding lattice. DFT calculations with polymorphic structures suggest a significantly more stable perovskite than indicated by monomorphic structures. FAPbI₃ may decompose into constituents PbI₂ and FAI (ΔH_{decomp} , reaction R1). From our polymorphic calculations, $\Delta H_{\text{decomp,poly}} = 0.01$ eV, whereas from our monomorphic calculations, $\Delta H_{\text{decomp,mono}} = -0.12$ eV. ΔH_{decomp} could be augmented by rotational entropy, thermal energy, and the stabilizing influence of Cs (ca. +100 meV) not included here. Instead of decomposing completely, the perovskite may expel FAI and form Schottky defects ($\Delta H_{\text{Schottky}}$, reaction R2), consume Schottky defects, and form PbI₂ (ΔH_{PbI_2} , reaction R3) or perform either process in reverse. Walsh et al. calculated a Schottky formation enthalpy for dilute defects in MAPbI₃ of $\Delta H_{\text{Schottky,mono}} = 0.08$ eV, resulting in an equilibrium concentration of defects at 300 K of $\sim 219/\text{cm}^3$ ($y = 3.82\%$ of sites). $\Delta H_{\text{Schottky,mono}}$ is low, implying that high defect concentrations (y in (FAI)_{1-y}PbI₂ = 1–10%) could be stable^{38,46,48–50}



At the defect concentration estimated above, it may be inferred that interactions between defects are significant, and these interactions can be probed by changing the distance between V'_{FA} and V_I (Table 1). From our DFT calculations on FAPbI₃, $\Delta H_{\text{Schottky,mono}}$ are -0.06 and -0.36 eV when the defects are $a\frac{\sqrt{2}}{2}$ and $a\frac{\sqrt{5}}{2}$ away from one another, respectively; a is the pseudo-cubic lattice constant. Our $\Delta H_{\text{Schottky,poly}}$ are 0.81 and 0.80 eV, respectively. In both cases, further separation of the

Table 1. Calculated Reaction Enthalpies and Volumes from DFT for $\text{FAPbI}_3 \rightarrow \text{PbI}_2 + \text{FAI}$ (ΔH_{decomp}), $\text{FAPbI}_3 \rightarrow \text{V}_I^\bullet + \text{V}'_{\text{FA}} + \text{FAI}$ ($\Delta H_{\text{Schottky}}$), and $\text{V}_I^\bullet + \text{V}'_{\text{FA}} \rightarrow \text{PbI}_2$ (ΔH_{PbI_2})^a

	ΔH_{decomp} (eV)	$\Delta H_{\text{Schottky}}$ (eV)	ΔH_{PbI_2} (eV)	V (Å ³)	ΔV for $y = 1\%$
monomorphic	-0.12			279.8	
with V_I and V'_{FA} $a\frac{\sqrt{2}}{2}$ apart		-0.06	-0.06	279.0	-0.023
with V_I and V'_{FA} $a\frac{\sqrt{5}}{2}$ apart		-0.36	0.24	271.1	-0.248
polymorphic	0.01			270.9	
with V_I and V'_{FA} $a\frac{\sqrt{2}}{2}$ apart		0.81	-0.80	269.9	-0.029
with V_I and V'_{FA} $a\frac{\sqrt{5}}{2}$ apart		0.80	-0.78	269.0	-0.056

^aTotal cell volume is given for all structures, and change in the cell volume per 1% defect concentration is given for the Schottky defect structures.

defects is preferred, despite electrostatic attraction. $\Delta H_{\text{Schottky,poly}}$ supports very small defect concentrations. Figure 1 shows the relaxed atomic structures, and Table 1 shows the reaction enthalpies and unit cell volumes from the DFT calculations.

The lines separating the monomorphic and polymorphic structures become blurred in the defect calculations, as exhibited by narrowing differences in V_{DFT} . The monomorphic structures exhibit FA cations rotating away from their initial 100 directions (Figure 1b,c), whereas the polymorphic structures show some alignment of FA cations (Figure 1e,f). The structure that started monomorphic with a larger distance between the vacancies had the lowest total energy of any of the defect structures. V_{exp} and ΔV_{exp} during testing are shown broken down by test condition in Figure 4. V_{DFT} was larger

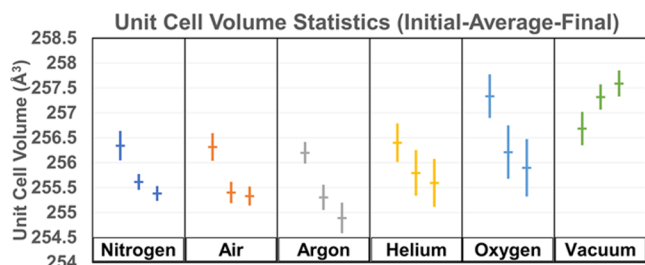


Figure 4. Comparison of mean and standard deviation values for initial, average, and final unit cell volumes of the perovskite phase measured over 50 h tests for each sample by testing condition shows that the perovskite lattice expands under vacuum testing but contracts under air or any flowing gas.

than V_{exp} in all cases, but there is a clear reduction in V_{DFT} when the defects are introduced. $\Delta V_{\text{DFT}} = -0.023$ and -0.029% for $\gamma = 1\%$. Volume changes explain energetic differences as the strain can be more evenly distributed when the vacancies are separated resulting in more negative ΔV_{DFT} than observed when vacancies are adjacent to each other. The reduction increased to $\Delta V_{\text{DFT}} = -0.056\%$ for a polymorphic structure with a greater distance between $V_{\text{FA}'}$ and V_{I} .

In tests under vacuum, the perovskite lattice expands, which is opposite to the lattice contraction observed for all other test conditions. The observed ΔV_{exp} over the course of the 50 h tests consistently falls within the range of $\Delta V_{\text{exp}} = -1.1 \pm 0.5$

\AA^3 for all flowing gases and atmospheres corresponding to an increase in the defect concentration of $\Delta\gamma = 4.2\text{--}27.2\%$ based on the range of DFT lattice contractions for 1% defect concentrations discussed above. In the vacuum tests, the perovskite lattice is observed to expand $\Delta V_{\text{exp}} = 0.9 \pm 0.3 \text{\AA}^3$ corresponding to a reduction in the defect concentration of $\Delta\gamma = -4.2$ to -20.4% .

In the fabrication procedure used for this study, the MHP thin film is crystallized at $\sim 140^\circ\text{C}$ and the substrate is then transferred to a room-temperature surface. This cools the substrate rapidly, a form of quenching. Quenching a crystal freezes in higher concentrations of defects than are thermodynamically ideal at the lower temperature.

Crystallization temperature and cooling rate are both highly uniform for samples cut from the same substrate. Crystal formation is rapid, occurring within seconds of placing the substrate on the hotplate. For $V_{\text{FA}'}/V_{\text{I}}$ Schottky-type defects, given $\Delta H_{\text{Schottky,mono}} = 0.08 \text{ eV}$, the equilibrium concentration at 140°C is $\gamma = 9.34\%$, more than double the equilibrium value at room temperature.³⁸ Local stoichiometric variations exist in the films prior to crystallization. These heterogeneities represent a spatially varying chemical potential, which can overcome $\Delta H_{\text{Schottky,poly}}$. $\Delta H_{\text{decomp,poly}}$ and $\Delta H_{\text{Schottky,poly}}$ suggest that MHP films do not necessarily contain minority phases or high γ -values as intrinsic characteristics; instead, both could be a consequence of nonstoichiometry with observed defect concentrations being metastable.

Since clear first-order behavior was not observed under atmosphere or flowing gas conditions, even after 50 h of degradation, we selected one sample on which to run an extended degradation experiment (Figure 5). Sample IV-B was subjected to three additional test cycles under lab atmosphere, a total of 200 h of irradiation, long enough that all perovskite signal was lost. I_{FAPbI_3} dropped below 10% of initial at ~ 60 h, at which point I_{PbI_2} began to decrease indicating additional degradation processes. SEM investigation of IV-B after the extended testing showed significant loss of material compared to another sample from the same substrate IV-A (Figure 5).

I_{FAPbI_3} and I_{PbI_2} trajectories are shown for selected gas conditions applied to samples (Figure 6b). In all of the tests under atmosphere or flowing gas, the loss of perovskite and growth of PbI_2 are constant over the duration of the

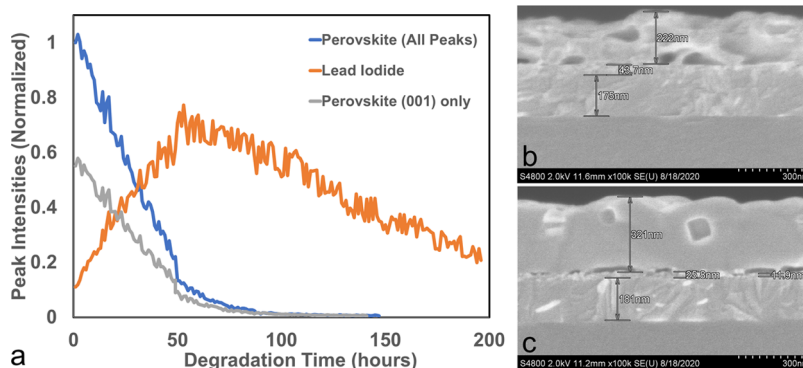


Figure 5. Changes over extended testing in air. (a) Perovskite and PbI_2 signal intensity trajectories for an extended degradation test under atmospheric diffusion. Once the perovskite is nearly all gone, the PbI_2 signal intensity begins to decrease. The plot shows that the nature of the degradation processes under nonvacuum conditions is not actually zeroth order, but that the higher-order rate behavior does not manifest until the perovskite is almost entirely degraded. (b) Cross-sectional SEM of sample IV-B taken after the extended testing in air and (c) comparison SEM after nitrogen-flow testing of sample IV-Ad.

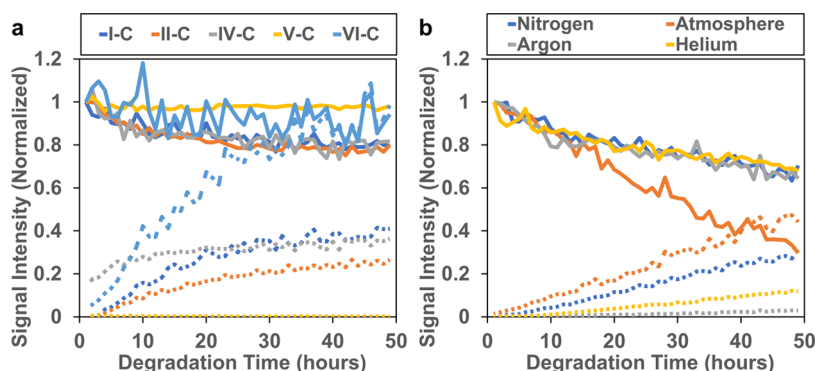


Figure 6. Intensity trajectories of the perovskite (solid lines) and PbI_2 (dashed lines) in (a) all vacuum tests and (b) example air, argon, nitrogen, and helium tests illustrate the difference in apparent kinetic order of the degradation processes under vacuum compared to other test conditions. Intensities are normalized to the initial perovskite intensity for each test.

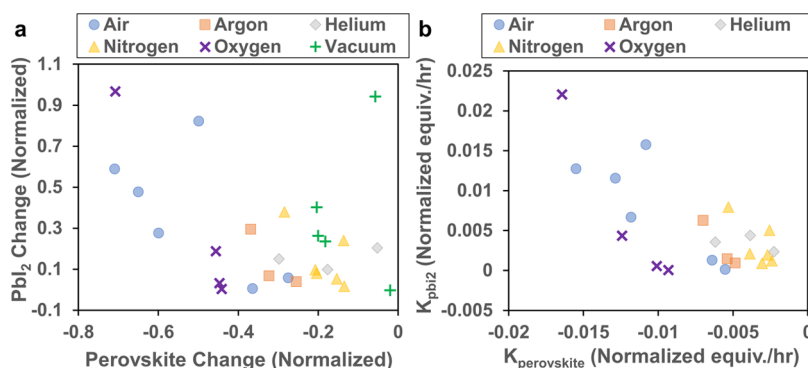


Figure 7. (a) Total changes of perovskite vs PbI_2 signal intensities over the testing period normalized to the initial perovskite intensity for all tests, (b) zeroth-order rate constants for perovskite loss vs PbI_2 growth processes for all nonvacuum tests. These plots illustrate that perovskite loss and PbI_2 growth are correlated and of similar magnitude but do not directly correspond to one another. This illustrates that not all perovskite loss results in PbI_2 growth nor vice versa. The plots further illustrate that perovskite loss rates are higher under O_2 and atmosphere than in other conditions. Normalization of these data was done to improve the comparability of data and is based on the perovskite signal intensity from the first measurement of each test.

experiments—appearing to obey zeroth-order rate laws with respect to I_{FAPbI_3} or I_{PbI_2} , and plots of intensity vs time being straight lines. This probably indicates that the limiting component of perovskite loss is the X-ray flux. By contrast, in all but one test under vacuum conditions, perovskite loss and PbI_2 growth obey first-order rate laws, as indicated by the curves of the intensity vs time plots of I_{FAPbI_3} and I_{PbI_2} . The measured total perovskite loss in the vacuum tests, 7.1–29.7%, agrees well with the estimated reduction in Schottky defect concentration (c.f. reaction R3). The outlier vacuum test result was unusually stable and showed no significant change in peak intensities over the 50 h test period.—

Slopes from linear fits give rate constants k_{FAPbI_3} and k_{PbI_2} in tests under flowing gas or atmosphere (Figure 7). Under lab atmosphere and oxygen flow conditions, we observe the accelerated loss of I_{FAPbI_3} compared to He, N_2 , Ar, and vacuum. In vacuum tests, I_{FAPbI_3} and I_{PbI_2} approach equilibrium conditions with nonzero perovskite signals (Figure 6a). To determine rate constants for tests under vacuum, it was necessary to express each of the rate functions in the form of (eq 1), where $[A]$ is the concentration of A (FAPbI_3 and PbI_2 concentrations are proportionally related to the diffracted signal intensity) at time t , $[A_x]$ is the concentration at equilibrium, $[A_0]$ is the change in concentration from $t = 0$ to equilibrium, and k is the rate constant. Values for $[A_0]$, $[A_x]$,

and k were then refined to fit the experimental data. Tables of k_{FAPbI_3} and k_{PbI_2} for all tests are available in the Supporting Information (Tables S3 and S4)

$$[A](t) = [A_x] + [A_0] \times \exp(-k \times t) \quad (1)$$

Attenuation lengths for 8.04 keV X-rays at atmospheric pressure for He, N_2 , Air, O_2 , and Ar are 20 493, 111.2, 101.7, 63.5, and 4.88 cm, respectively.⁵¹ The beam path length of 6 cm within the chamber results in the loss of <5% of X-ray intensity in all gases except argon. An estimated attenuation length based on density for Cu $K\alpha$ X-rays within the perovskite film is 9.986 μm , much longer than the perovskite layer thickness (<375 nm).⁵¹ These values indicate that X-ray absorption is uniform throughout the perovskite layer in all tests and should be nearly identical between all test conditions other than Ar flow. Notably, k_{FAPbI_3} and k_{PbI_2} under Ar flow are quite high, indicating that the X-ray absorption by the gas may be more important than the perovskite X-ray absorption for determining reaction rates.

Approximate rates of ionization of the particles in each gas from the X-ray beam can be found using the X-ray photon energy, the incident beam power, and the ionization energy and attenuation properties of the gas. Ionization energies range from 12.18 eV for oxygen to 24.58 eV for helium.⁵² Cu source X-ray production has an energy efficiency of ~1%; our source was operated at 600 W, giving an intensity of ~6 W. Incident

optics in our setup should attenuate that by not more than 75%, giving us an estimated beam flux of 1.5 W onto an area of 1 cm². Compton scattering angles greater than 30° are sufficient for 8.04 keV photons to ionize any of the gases used in this study. Using the attenuation length values above, we estimate that the ionization rate of the test gases in the beam path (~3 cm × 1 cm × 0.1 cm) has the lowest rates for helium (between 1.4 × 10¹¹/s and 4.5 × 10¹³/s) and the largest rates for argon (between 4.3 × 10¹⁴/s and 2.2 × 10¹⁷/s). Ranges given are from a minimum of 1 ionization per attenuated photon to a maximum of full attenuated energy ionizing gas particles. The approximate number of formula units of FAPbI₃ perovskite in a 375 nm thick 1 cm square area is 1.5 × 10¹⁷.

The fact that k_{FAPbI_3} and k_{PbI_2} are zeroth-order terms under all test conditions except vacuum indicates that these processes are rate-limited by a species that is replenished under all test conditions except vacuum and formed at the surface of the perovskite through interaction with gas-phase species. As an ionic solid, the most common types of point defects in FAPbI₃ perovskite are charge-balanced: Schottky defects (paired cation and anion vacancies) and Frenkel defects (an ion vacancy and interstitial).²⁰

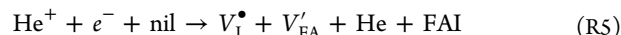
Frenkel V_i/I_i' defect concentrations above equilibrium levels can be eliminated purely by ion migration. Light exposure has been shown to have an influence on ion migration in lead halide MHPs. Mosconi et al. found that photoluminescence dynamics under illumination could be attributed to the local elimination of V_i/I_i' Frenkel-type defects, which they report as having a corrected formation energy of 0.69 eV, giving an equilibrium concentration at 300 K of ~10¹⁰/cm³ (or ~7.67 × 10⁻¹⁰% of sites).^{6,20} We speculate that, in our tests, the absorption of X-rays in the perovskite is promoting ion migration, at least partially by excited-state destabilization of Frenkel defects.^{4,53}

Removing excess concentrations of V_{FA}'/V_i Schottky-type defects requires either the addition of FAI or removal of PbI₂ from the perovskite component of the sample, in addition to ion migration. Expulsion of Schottky defects is then dependent on the presence or the formation of minority phases in contact with the MHP and a sufficiently high ion mobility for the defects to reach these minority phases.

The behaviors we observe in our vacuum tests match well with a process of eliminating excess V_{FA}'/V_i Schottky-type defects from the perovskite phase by ion migration and the formation of PbI₂. This is evidenced by the loss of perovskite signal and the growth of the PbI₂ signal. As the excess Schottky defect concentration is eliminated, k_{FAPbI_3} and k_{PbI_2} slow. The lattice expansion observed in vacuum tests is likely another consequence of lowering the y -value. In the vacuum tests, the measured perovskite loss and PbI₂ gain are close in magnitude to the estimated reduction of Schottky defect concentrations from ΔV_{exp} . As mentioned previously, one of the vacuum-tested samples showed no PbI₂ signal growth and the perovskite signal increased slightly throughout the experiment but did undergo lattice expansion. The behavior of this outlier sample can be explained if FAI-rich minority phases existed adjacent to the crystallite domains (e.g., anterior surface, grain boundary). The Schottky defects would then be eliminated by FAI incorporation into the perovskite without requiring PbI₂ formation or the loss of perovskite signal (reaction R2), a process fits well with the atomic-scale microscopy observations of stable FA-vacancies at perovskite surfaces by Rothmann et

al.⁷ Plots showing V_{exp} , I_{FAPbI_3} , and I_{PbI_2} of all samples are available in the Supporting Information (Figures S6–S10).

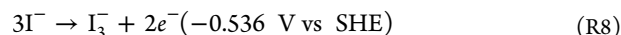
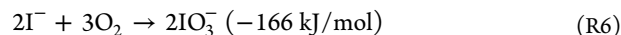
With gases in the sample chamber, reactive pathways become available, which drive the system toward continuous vacancy production and continuous perovskite loss. Electrons are ejected from the gas-forming cations (reaction R4) such as He⁺. The ionized gas then reacts with surface formamidinium and iodine ions forming Schottky defects by extracting FAI (reaction R5)



The process of V_{FA}'/V_i Schottky defect production at the sample surface under inert gas and atmosphere creates a y -value gradient. Ion migration promoted by the impinging X-rays then leads to increased Schottky defect concentration in the bulk of the crystal. Increasing the y -value is expected to cause lattice contraction just as decreasing the y -value leads to lattice expansion.

Removal of iodide and formamidinium, in turn, drives PbI₂ production (reaction R3); however, this does not explain PbI₂ and overall diffraction signal loss. Oxygen provides an accelerated degradation pathway, possibly due to iodate formation. Formation of nondiffracting PbO has been observed in MHP films by Raman spectroscopy following proton irradiation and could be a contributing factor.⁵ Iodide photo-oxidation to iodate is a known process and could be accelerated under the X-ray flux.⁵⁴ There are four possible oxyiodo-species that could form: hypoiodite, iodite, iodate, and periodate. The reaction for the formation of iodate is given as an example with ΔG^0 in parentheses (reaction R6).

Concurrent environmental XPS stability investigations with cesium-containing FAPbI₃ thin films, in collaboration with the Colorado School of Mines, revealed that exposure to X-ray photons results in Pb⁰ formation (reaction R7).⁸ Additionally, a common degradation mode for iodide-containing species involves oxidation to the triiodide species (reaction R8). The specific role of both processes in MHP degradation is a focus of ongoing work within our group



The loss of the PbI₂ signal does not correspond to an increase in any other diffracted signal, indicating that whatever decay products are being formed from PbI₂, they are amorphous, gaseous, or are nanoparticles too small to give an identifiable diffraction signal. Other studies have observed the formation of Pb metal from lead halide perovskite samples under either X-ray irradiation or elevated temperature.^{50,55} It is possible that the system is forming some nanoparticulate Pb metal, though the (111) Pb metal diffraction peak—the only Pb metal peak that falls within the 2θ range of our measurements—is not observed. Generation of iodate ions allows the formation of amorphous lead iodate salts as alternative degradation pathways to PbI₂ formation, which would explain the disparity in k_{FAPbI_3} and k_{PbI_2} seen in tests under atmosphere and flowing oxygen.

The presence of oxygen merely accelerates the net perovskite loss reaction, changing the perovskite lattice in

the same way as the inert gas. The effect of oxygen is subject to the same limitation to γ -values as in the inert gas and results in the same ΔV_{exp} . The differences in reactivity in the vacuum (reaction R3), inert gas flow (reactions R3–R5), and oxygen (reactions R3–R6) are exhibited as different k_{FAPbI_3} , as measured by XRD. It should be noted that elemental iodine does not appear in the diffraction patterns of degradation experiments. The vapor pressure of elemental iodine at 75 °C is 1.62 kPa, so it is possible that the excess iodine is off-gassing from the sample fast enough that it does not accumulate in appreciable quantities. The formation of gaseous species during degradation processes will be the subject of future studies.

Low $\Delta H_{\text{decomp,mono}}$ and $\Delta H_{\text{Schottky,mono}}$ present a picture of high concentrations of intrinsic defects and minority phases, which are continually replenished by perovskite degradation, linking the stability of the perovskite to the stability of its minority phases. In sharp contrast, high $\Delta H_{\text{decomp,ooly}}$ and $\Delta H_{\text{Schottky,poly}}$ present a more optimistic view of high intrinsic perovskite stability.

CONCLUSIONS

In this study, we used powder X-ray diffraction to monitor changes to formamidinium lead iodide perovskite thin films, which were subjected to ionizing radiation exposure (X-rays) at elevated temperature, under a variety of atmospheric conditions for 50 h test periods. Our results indicate that formamidinium lead iodide perovskite materials are not only stabilized under vacuum against degradation from ionizing radiation but actively expel defects from the crystalline bulk. Under other atmospheric conditions, there is an additional process that results in the continuous loss of material from the perovskite, a process presumably driven by ionization of the gases at the perovskite surface.

Our results here support the well-established theory that defect-mediated ion migration is a fundamental driver for lead halide perovskite degradation.^{26,27} However, key insights are afforded by this work into the requirements for mobile ion transfer out of the perovskite, namely, the extraction of I^- and FA^+ ions from the perovskite surface requires the action of a mediator. Even nominally inert gases, once ionized, can fill the role of mediator and damage the perovskite. With exposure to ionizing radiation, the degradation of bare MHP films is progressive even under a flowing helium gas.

We found that, under X-ray irradiation, the perovskite lattice expands in vacuum but contracts in all tested gases. The lattice contractions are attributed to an increase in V_{FA^+} and V_{I} concentrations in the perovskite driven by the extraction of I^- and FA^+ ions mediated by ionized gases or related reactive byproducts. The lattice expansion observed under vacuum is attributed to the elimination of V_{FA^+} and V_{I} as increased ion mobility under testing conditions brings defect concentrations closer to equilibrium levels with the associated formation of PbI_2 .

While ion migration plays an important role in the degradation process, it appears to be a net benefit to the long-term stability of the perovskite. Because of ion migration redistributing vacancy sites away from the surface of the material, the perovskite crystal structure is retained even under significant ion loss.⁷ The perovskite can eliminate excess site vacancies by absorbing replacement ions, if they are present, or by forming PbI_2 at the perovskite surface. The cyclic damage

and recovery process are illustrated by subsequent lattice expansion and contraction of the same film when exposed to the first vacuum and then flowing oxygen and by contraction followed by expansion in a sample first subjected to flowing argon followed by vacuum. The elevated temperatures used for crystallizing the perovskite cause it to form with a high, metastable defect concentration. In vacuum, this concentration decreases, moving toward equilibrium.

Careful examination of perovskite stability via the lens of majority/minority phases and defects illustrates that perovskites have a bright future. High defect concentrations are only possible due to the fabrication conditions or continuous excitation-driven loss of ions from the perovskite itself. Our calculations indicate that the equilibrium defect concentrations are quite low. However, the results suggest that there can be amorphous FAI-rich minority phases contained within solution-processed MHP thin films that can act as a buffer against material loss from the perovskite or a sink for the expulsion of defects, once the defects have been mobilized. Taken together, the data indicate that the MHP materials studied here are quite robust against degradation. We find that efforts to improve the long-term stability of MHP devices should focus on developing adjacent layers or interlayer surface treatments to inhibit the migration of mobile ions away from the perovskite surface.

EXPERIMENTAL SECTION

X-ray diffraction measurements were performed using a Rigaku Miniflex 600 benchtop diffractometer operating in the Bragg–Brentano geometry with an Anton Paar BTS 500 heated, controlled atmosphere stage. Flowing gases were passed through the stage at a rate of ~ 5 mL/s. The BTS 500 sample chamber is semicircular with a radius of ~ 3.5 cm. The volume of the chamber is ~ 23 mL. For lab atmosphere tests, the gas inlet and outlet ports of the stage were left open. Lab atmospheric conditions on the days of the tests are given in Table S4. For vacuum tests, a pump rated to pull a vacuum of 0.02 Torr was attached to the inlet port and the outlet port was sealed.

Diffraction scans were collected using copper $K\alpha$ radiation (45 kV, 15 mA) with an SC-70 detector measuring from 5 to 35° 2θ at a scan rate of 0.5°/min with a 0.02° step width in a continuous collection mode. Diffractometer optics used included 1.25° divergence slits, 0.3 mm receiving slit, 5.0° Soller slits, and one Cu $K\beta$ filter (Ni-foil). Thin film surfaces were perpendicular to the plane of reflection for all measurements. The scan range covers five peaks in the cubic FAPbI_3 diffraction pattern (001, 011, 111, 002, and 012) as well as two peaks in the diffraction pattern of the ITO conducting layer on the substrates. Intensities of diffraction signals for each test are normalized to the initial perovskite diffraction intensity (first scan of test) when comparing I_{FAPbI_3} and I_{PbI_2} .

Flat specimen and sample displacement angle corrections were applied to the measured diffraction patterns to account for angle shifts arising from the thin film nature of the samples and for a variability in sample position that the experimental setup prevented us from eliminating mechanically. The functional forms of the flat specimen and sample displacement angle corrections are available in the Supporting Information along with displacement parameters used in our analysis.

The MHP films tested in this study are FAPbI_3 -amalgamated with <5 mol % Cs^+ . The perovskite thin films used in this experiment were grown by a two-step blade-coating fabrication method described elsewhere.^{56–58} Perovskite films were deposited on top of a layer of nickel oxide on ITO-coated glass substrates (as the bottom half of analogue for solar cell devices with the P–I–N architecture).⁶⁰ Perovskite films were fabricated on 50 mm \times 50 mm square substrates, which were then cut into four sections that could each fit

into the BTS 500 XRD stage. A total of 25 thin film samples were used in this study from 7 substrates.⁶⁰

DFT calculations were performed with the Vienna ab initio software package (VASP).^{59,61} Stoichiometric and Schottky defect calculations were performed using $2 \times 2 \times 2$ (8 perovskite formula unit) supercells. The electronic structure was calculated using a 500 eV plane-wave cutoff and a $7 \times 7 \times 7$ γ -centered Monkhorst–Pack mesh.⁶² The Perdew–Burke–Ernzerhof (PBE) form of the generalized gradient approximation (GGA) was applied for the calculation of exchange–correlation energy.⁶³ All structures were relaxed until atomic forces were less than 0.01 eV/Å. Cell lengths, angles, and atomic positions were all allowed to relax for all structures. The achieved final structures should be interpreted as a local minimum attractor, which the initial structure relaxed into. Six FAPbI₃ structures in addition to crystalline FAI and PbI₂ were used in these calculations.

■ ASSOCIATED CONTENT

SI Supporting Information

The Supporting Information is available free of charge at <https://pubs.acs.org/doi/10.1021/acsami.1c24709>.

Tables of sample test conditions, XRD error correction values by test, laboratory atmospheric conditions during testing, and derived rate constants for each test; figures include final vs initial unit cell volumes, post-testing photography of all samples, plotted diffraction patterns from each test cycle, plots of perovskite peak *d*-spacing trajectories (as in Figure 2) for each test, post-testing photoluminescence spectra for each sample, photographs of two as-fabricated substrates prior to being cut into sample quadrants, post-testing SEM images of selected samples, scatter plots comparing initial perovskite 001 peak intensities and initial PbI₂ peak intensities to degradation rate constants; and notes detailing error correction procedures and geometrical relationships for rhombohedral lattice as distortion from cubic (PDF)

Measured XRD data 1 of 2 (XLSX)

Measured XRD data 2 of 2 (XLSX)

■ AUTHOR INFORMATION

Corresponding Author

Michael D. Irwin – CubicPV Inc., Dallas, Texas 75201, United States; Email: mirwin@cubicpv.com

Authors

Michael Holland – CubicPV Inc., Dallas, Texas 75201, United States; orcid.org/0000-0002-7491-9998

Anthony Ruth – CubicPV Inc., Dallas, Texas 75201, United States

Kamil Mielczarek – CubicPV Inc., Dallas, Texas 75201, United States

Vivek V. Dhas – CubicPV Inc., Dallas, Texas 75201, United States

Joseph J. Berry – National Renewable Energy Laboratory, Golden, Colorado 80401, United States

Complete contact information is available at: <https://pubs.acs.org/doi/10.1021/acsami.1c24709>

Notes

The authors declare the following competing financial interest(s): Authors Michael Holland, Anthony Ruth, Vivek Dhas, and Michael Irwin are employed by CubicPV Inc., a manufacturer of solar photovoltaic equipment and materials.

■ ACKNOWLEDGMENTS

The authors wish to thank D. Westley Miller and N. C. Anderson for helpful suggestions and discussions. This work was self-funded by CubicPV Inc. and previously by Hunt Perovskite Technologies LLC.

■ REFERENCES

- (1) Lee, M. M.; Teuscher, J.; Miyasaka, T.; Murakami, T. N.; Snaith, H. J. Efficient Hybrid Solar Cells Based on Meso-Superstructured Organometal Halide Perovskites. *Science* **2012**, *338*, 643–647.
- (2) Wei, H.; Huang, J. Halide Lead Perovskites for Ionizing Radiation Detection. *Nat. Commun.* **2019**, *10*, No. 1066.
- (3) Boyd, C. C.; Cheacharoen, R.; Leijtens, T.; McGehee, M. D. Understanding Degradation Mechanisms and Improving Stability of Perovskite Photovoltaics. *Chem. Rev.* **2019**, *119*, 3418–3451.
- (4) Miyazawa, Y.; Ikegami, M.; Chen, H.-W.; Ohshima, T.; Imaizumi, M.; Hirose, K.; Miyasaka, T. Tolerance of Perovskite Solar Cell to High-Energy Particle Irradiations in Space Environment. *iScience* **2018**, *2*, 148–155.
- (5) Martínez, W. O. H.; Giudici, P.; Correa Guerrero, N. B.; Ibarra, M. L.; Perez, M. D. Effect of High Energy Proton Irradiation on MAPbI₃ Films for Space Applications Observed by Micro-Raman Spectroscopy. *Mater. Adv.* **2020**, *1*, 2068–2073.
- (6) Mosconi, E.; Meggiolaro, D.; Snaith, H. J.; Stranks, S. D.; De Angelis, F. Light-Induced Annihilation of Frenkel Defects in Organolead Halide Perovskites. *Energy Environ. Sci.* **2016**, *9*, 3180–3187.
- (7) Rothmann, M. U.; Kim, J. S.; Borchert, J.; Lohmann, K. B.; O'Leary, C. M.; Shearer, A. A.; Clark, L.; Snaith, H. J.; Johnston, M. B.; Nellist, P. D.; Herz, L. M. Atomic-Scale Microstructure of Metal Halide Perovskite. *Science* **2020**, *370*, No. eabb5940.
- (8) Donakowski, A.; Miller, D. W.; Anderson, N. C.; Ruth, A.; Sanehira, E. M.; Berry, J. J.; Irwin, M. D.; Rockett, A.; Steirer, K. X. Improving Photostability of Cesium-Doped. *ACS Energy Lett.* **2021**, *6*, 574–580.
- (9) Li, W.; Sun, Y. Y.; Li, L.; Zhou, Z.; Tang, J.; Prezhdo, O. V. Control of Charge Recombination in Perovskites by Oxidation State of Halide Vacancy. *J. Am. Chem. Soc.* **2018**, *140*, 15753–15763.
- (10) Koutná, N.; Holec, D.; Svoboda, O.; Klimashin, F. F.; Mayrhofer, P. H. Point Defects Stabilize Cubic Mo-N and Ta-N. *J. Phys. D: Appl. Phys.* **2016**, *49*, No. 375303.
- (11) Kerner, R. A.; Rand, B. P. Ionic-Electronic Ambipolar Transport in Metal Halide Perovskites: Can Electronic Conductivity Limit Ionic Diffusion? *J. Phys. Chem. Lett.* **2018**, *9*, 132–137.
- (12) Moia, D.; Gelmetti, I.; Calado, P.; Fisher, W.; Stringer, M.; Game, O.; Hu, Y.; Docampo, P.; Lidzey, D.; Palomares, E.; Nelson, J.; Barnes, P. R. F. Ionic-to-Electronic Current Amplification in Hybrid Perovskite Solar Cells: Ionically Gated Transistor-Interface Circuit Model Explains Hysteresis and Impedance of Mixed Conducting Devices. *Energy Environ. Sci.* **2019**, *12*, 1296–1308.
- (13) Zarazua, I.; Bisquert, J.; Garcia-Belmonte, G. Light-Induced Space-Charge Accumulation Zone as Photovoltaic Mechanism in Perovskite Solar Cells. *J. Phys. Chem. Lett.* **2016**, *7*, 525–528.
- (14) Knight, A. J.; Wright, A. D.; Patel, J. B.; McMeekin, D. P.; Snaith, H. J.; Johnston, M. B.; Herz, L. M. Electronic Traps and Phase Segregation in Lead Mixed-Halide Perovskite. *ACS Energy Lett.* **2019**, *4*, 75–84.
- (15) Hutter, E. M.; Muscarella, L. A.; Wittmann, F.; Versluis, J.; McGovern, L.; Bakker, H. J.; Woo, Y.-W.; Jung, Y.-K.; Walsh, A.; Ehrler, B. Thermodynamic Stabilization of Mixed-Halide Perovskites against Phase Segregation. *Cell Rep. Phys. Sci.* **2020**, *1*, No. 100120.
- (16) Yang, J. H.; Yin, W. J.; Park, J. S.; Wei, S. H. Fast Self-Diffusion of Ions in CH₃NH₃PbI₃: The Interstitially Mechanism: Versus Vacancy-Assisted Mechanism. *J. Mater. Chem. A* **2016**, *4*, 13105–13112.
- (17) Zhang, H.; Fu, X.; Tang, Y.; Wang, H.; Zhang, C.; Yu, W. W.; Wang, X.; Zhang, Y.; Xiao, M. Phase Segregation Due to Ion Migration in All-Inorganic Mixed-Halide Perovskite Nanocrystals. *Nat. Commun.* **2019**, *10*, No. 1088.

- (18) Eames, C.; Frost, J. M.; Barnes, P. R. F.; O'Regan, B. C.; Walsh, A.; Islam, M. S. Ionic Transport in Hybrid Lead Iodide Perovskite Solar Cells. *Nat. Commun.* **2015**, *6*, No. 7497.
- (19) Elmelund, T.; Scheidt, R. A.; Seger, B.; Kamat, P. V. Bidirectional Halide Ion Exchange in Paired Lead Halide Perovskite Films with Thermal Activation. *ACS Energy Lett.* **2019**, *4*, 1961–1969.
- (20) Meggiolaro, D.; Mosconi, E.; De Angelis, F. Formation of Surface Defects Dominates Ion Migration in Lead-Halide Perovskites. *ACS Energy Lett.* **2019**, *4*, 779–785.
- (21) Schelhas, L. T.; Li, Z.; Christians, J. A.; Goyal, A.; Kairys, P.; Harvey, S. P.; Kim, D. H.; Stone, K. H.; Luther, J. M.; Zhu, K.; Stevanovic, V.; Berry, J. J. Insights into Operational Stability and Processing of Halide Perovskite Active Layers. *Energy Environ. Sci.* **2019**, *12*, 1341–1348.
- (22) Yuan, Y.; Chae, J.; Shao, Y.; Wang, Q.; Xiao, Z.; Centrone, A.; Huang, J. Photovoltaic Switching Mechanism in Lateral Structure Hybrid Perovskite Solar Cells. *Adv. Energy Mater.* **2015**, *5*, No. 1500615.
- (23) Li, C.; Guerrero, A.; Huettner, S.; Bisquert, J. Unravelling the Role of Vacancies in Lead Halide Perovskite through Electrical Switching of Photoluminescence. *Nat. Commun.* **2018**, *9*, No. 5113.
- (24) Meloni, S.; Moehl, T.; Tress, W.; Frankevičius, M.; Saliba, M.; Lee, Y. H.; Gao, P.; Nazeeruddin, M. K.; Zakeeruddin, S. M.; Rothlisberger, U.; Grätzel, M. Ionic Polarization-Induced Current-Voltage Hysteresis in CH₃NH₃PbX₃ Perovskite Solar Cells. *Nat. Commun.* **2016**, *7*, No. 10334.
- (25) Draguta, S.; Sharia, O.; Yoon, S. J.; Brennan, M. C.; Morozov, Y. V.; Manser, J. M.; Kamat, P. V.; Schneider, W. F.; Kuno, M. Rationalizing the Light-Induced Phase Separation of Mixed Halide Organic-Inorganic Perovskites. *Nat. Commun.* **2017**, *8*, No. 200.
- (26) Kim, S.; Bae, S.; Lee, S. W.; Cho, K.; Lee, K. D.; Kim, H.; Park, S.; Kwon, G.; Ahn, S. W.; Lee, H. M.; Kang, Y.; Lee, H. S.; Kim, D. Relationship between Ion Migration and Interfacial Degradation of CH₃NH₃PbI₃ Perovskite Solar Cells under Thermal Conditions. *Sci. Rep.* **2017**, *7*, No. 1200.
- (27) Yuan, H.; Debroye, E.; Janssen, K.; Naiki, H.; Steuwe, C.; Lu, G.; Moris, M.; Orgiu, E.; Uji-I, H.; De Schryver, F.; Samorì, P.; Hofkens, J.; Roeffaers, M. Degradation of Methylammonium Lead Iodide Perovskite Structures through Light and Electron Beam Driven Ion Migration. *J. Phys. Chem. Lett.* **2016**, *7*, 561–566.
- (28) Kim, G. Y.; Senocrate, A.; Yang, T.-Y.; Gregori, G.; Grätzel, M.; Maier, J. Large Tunable Photoeffect on Ion Conduction in Halide Perovskites and Implications for Photodecomposition. *Nat. Mater.* **2018**, *17*, 445–449.
- (29) Bischak, C. G.; Hetherington, C. L.; Wu, H.; Aloni, S.; Ogletree, D. F.; Limmer, D. T.; Ginsberg, N. S. Origin of Reversible Photoinduced Phase Separation in Hybrid Perovskites. *Nano Lett.* **2017**, *17*, 1028–1033.
- (30) Calado, P.; Telford, A. M.; Bryant, D.; Li, X.; Nelson, J.; O'Regan, B. C.; Barnes, P. R. F. Evidence for Ion Migration in Hybrid Perovskite Solar Cells with Minimal Hysteresis. *Nat. Commun.* **2016**, *7*, No. 13831.
- (31) Motti, S. G.; Meggiolaro, D.; Barker, A. J.; Mosconi, E.; Perini, C. A. R.; Ball, J. M.; Gandini, M.; Kim, M.; De Angelis, F.; Petrozza, A. Controlling Competing Photochemical Reactions Stabilizes Perovskite Solar Cells. *Nat. Photonics* **2019**, *13*, 532–539.
- (32) Futscher, M. H.; Lee, J. M.; McGovern, L.; Muscarella, L. A.; Wang, T.; Haider, M. I.; Fakhruddin, A.; Schmidt-Mende, L.; Ehrler, B. Quantification of Ion Migration in CH₃NH₃PbI₃ Perovskite Solar Cells by Transient Capacitance Measurements. *Mater. Horiz.* **2019**, *6*, 1497–1503.
- (33) Feng, Y.; Zhao, Y.; Zhou, W. K.; Li, Q.; Saidi, W. A.; Zhao, Q.; Li, X. Z. Proton Migration in Hybrid Lead Iodide Perovskites: From Classical Hopping to Deep Quantum Tunneling. *J. Phys. Chem. Lett.* **2018**, *9*, 6536–6543.
- (34) Ruth, A.; Brennan, M. C.; Draguta, S.; Morozov, Y. V.; Zhukovskiy, M.; Janko, B.; Zapol, P.; Kuno, M. Vacancy-Mediated Anion Photo-segregation Kinetics in Mixed Halide Hybrid Perovskites: Coupled Kinetic Monte Carlo and Optical Measurements. *ACS Energy Lett.* **2018**, *3*, 2321–2328.
- (35) Weller, M. T.; Weber, O. J.; Frost, J. M.; Walsh, A. Cubic Perovskite Structure of Black Formamidinium Lead Iodide, α -[HC(NH₂)₂]PbI₃, at 298 K. *J. Phys. Chem. Lett.* **2015**, *6*, 3209–3212.
- (36) Kawachi, S.; Atsumi, M.; Saito, N.; Ohashi, N.; Murakami, Y.; Yamaura, J. Structural and Thermal Properties in Formamidinium and Cs-Mixed Lead Halides. *J. Phys. Chem. Lett.* **2019**, *10*, 6967–6972.
- (37) Bonn, M.; Miyata, K.; Hendry, E.; Zhu, X. Y. Role of Dielectric Drag in Polaron Mobility in Lead Halide Perovskites. *ACS Energy Lett.* **2017**, *2*, 2555–2562.
- (38) Walsh, A.; Scanlon, D. O.; Chen, S.; Gong, X. G.; Wei, S. H. Self-Regulation Mechanism for Charged Point Defects in Hybrid Halide Perovskites. *Angew. Chem., Int. Ed.* **2015**, *54*, 1791–1794.
- (39) Dalpian, G. M.; Zhao, X. G.; Kazmerski, L.; Zunger, A. Formation and Composition-Dependent Properties of Alloys of Cubic Halide Perovskites. *Chem. Mater.* **2019**, *31*, 2497–2506.
- (40) Azpiroz, J. M.; Mosconi, E.; Bisquert, J.; De Angelis, F. Defect Migration in Methylammonium Lead Iodide and Its Role in Perovskite Solar Cell Operation. *Energy Environ. Sci.* **2015**, *8*, 2118–2127.
- (41) Tao, S.; Schmidt, I.; Brocks, G.; Jiang, J.; Tranca, I.; Meerholz, K.; Olthof, S. Absolute Energy Level Positions in Tin- and Lead-Based Halide Perovskites. *Nat. Commun.* **2019**, *10*, No. 2560.
- (42) Pavlovic, I. M.; Brennan, M. C.; Draguta, S.; Ruth, A.; Moot, T.; Christians, J. A.; Aleshire, K.; Harvey, S. P.; Toso, S.; Nanayakkara, S. U.; Messinger, J.; Luther, J. M.; Kuno, M. K. Suppressing Cation Migration in Triple-Cation Lead Halide Perovskites. *ACS Energy Lett.* **2020**, *5*, 2802–2810.
- (43) Yi, C.; Luo, J.; Meloni, S.; Boziki, A.; Ashari-Astani, N.; Grätzel, M.; Zakeeruddin, S. M.; Rothlisberger, U.; Grätzel, M. Entropic Stabilization of Mixed A-Cation ABX₃ Metal Halide Perovskites for High Performance Perovskite Solar Cells. *Energy Environ. Sci.* **2016**, *9*, 656–662.
- (44) Du, M. H. Density Functional Calculations of Native Defects in CH₃NH₃PbI₃: Effects of Spin - Orbit Coupling and Self-Interaction Error. *J. Phys. Chem. Lett.* **2015**, *6*, 1461–1466.
- (45) Buin, A.; Pietsch, P.; Xu, J.; Voznyy, O.; Ip, A. H.; Comin, R.; Sargent, E. H. Materials Processing Routes to Trap-Free Halide Perovskites. *Nano Lett.* **2014**, *14*, 6281–6286.
- (46) Zhang, Y.-Y.; Chen, S.; Xu, P.; Xiang, H.; Gong, X.-G.; Walsh, A.; Wei, S.-H. Intrinsic Instability of the Hybrid Halide Perovskite Semiconductor CH₃NH₃PbI₃*. *Chin. Phys. Lett.* **2018**, *35*, No. 036104.
- (47) Yang, J. H.; Yin, W. J.; Park, J. S.; Wei, S. H. Self-Regulation of Charged Defect Compensation and Formation Energy Pinning in Semiconductors. *Sci. Rep.* **2015**, *5*, No. 16977.
- (48) Liu, N.; Yam, C. Y. First-Principles Study of Intrinsic Defects in Formamidinium Lead Triiodide Perovskite Solar Cell Absorbers. *Phys. Chem. Chem. Phys.* **2018**, *20*, 6800–6804.
- (49) Yin, W. J.; Shi, T.; Yan, Y. Unusual Defect Physics in CH₃NH₃PbI₃ Perovskite Solar Cell Absorber. *Appl. Phys. Lett.* **2014**, *104*, No. 063903.
- (50) Steirer, K. X.; Schulz, P.; Teeter, G.; Stevanovic, V.; Yang, M.; Zhu, K.; Berry, J. J. Defect Tolerance in Methylammonium Lead Triiodide Perovskite. *ACS Energy Lett.* **2016**, *1*, 360–366.
- (51) Chantler, C. T. Theoretical Form Factor, Attenuation, and Scattering Tabulation for Z = 1–92 from E = 1–10 EV to E = 0.4–1.0 MeV. *J. Phys. Chem. Ref. Data* **1995**, *24*, No. 71.
- (52) Sansonetti, J. E.; Martin, W. C. Handbook of Basic Atomic Spectroscopic Data. *J. Phys. Chem. Ref. Data* **2005**, *34*, 1559–2259.
- (53) Chen, S.; Gao, P. Challenges, Myths, and Opportunities of Electron Microscopy on Halide Perovskites. *J. Appl. Phys.* **2020**, *128*, No. 010901.
- (54) Sakurai, T. Photooxidation of Iodine Catalyzed by Uranyl Nitrate. *J. Nucl. Sci. Technol.* **1996**, *33*, 266–267.
- (55) Gao, X.; Ding, B.; Feng, Y.; Paul, J.; Gao, X.; Ding, B.; Kanda, H.; Fei, Z.; Luo, W.; Zhang, Y.; Tirani, F. F.; Scopelliti, R.; Kinge, S.;

et al. Engineering Long-Term Stability into Perovskite Solar Cells via Application of a Multi-Functional TFSI-Based Ionic Liquid Engineering Long-Term Stability into Perovskite Solar Cells via Application of a Multi-Functional TFSI-Based Ionic Liquid. *Cell Rep. Phys. Sci.* **2021**, *2*, No. 100475.

(56) Irwin, M. D.; Chute, J. A.; Dhas, V. V. Perovskite Material Layer Processing. U.S. Patent US9,425,396 B22016.

(57) Irwin, M. D.; Chute, J. A.; Dhas, V. V.; Mielczarek, K. Mixed Cation Perovskite Material Devices. U.S. Patent US10,316,196 B22019.

(58) Irwin, M. D.; Chute, J. A.; Dhas, V. V. Method of Formulating Perovskite Solar Cell Materials. U.S. Patent US9,305,715 B22016.

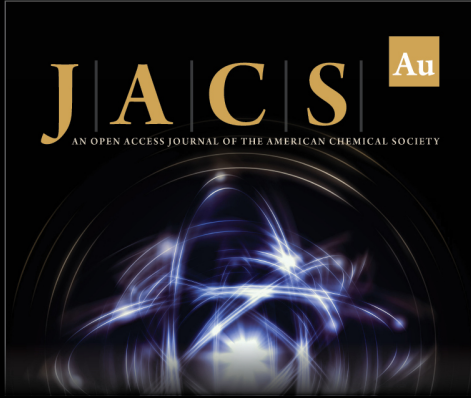
(59) Nandal, V.; Nair, P. R. Predictive Modeling of Ion Migration Induced Degradation in Perovskite Solar Cells. *ACS Nano* **2017**, *11*, 11505–11512.

(60) Irwin, M. D.; Dhas, V. V.; Mielczarek, K. Doped Nickel Oxide Interfacial Layer. U.S. Patent US10,189,998 B22019.

(61) Kresse, G.; Joubert, D. From Ultrasoft Pseudopotentials to the Projector Augmented-Wave Method. *Phys. Rev. B* **1999**, *59*, 1758–1775.


(62) Pack, J. D.; Monkhorst, H. J. “Special Points for Brillouin-Zone Integrations”—a Reply. *Phys. Rev. B* **1977**, *16*, 1748–1749.


(63) Perdew, J. P.; Burke, K.; Ernzerhof, M. Generalized Gradient Approximation Made Simple. *Phys. Rev. Lett.* **1996**, *77*, 3865–3868.



JACS Au
AN OPEN ACCESS JOURNAL OF THE AMERICAN CHEMICAL SOCIETY

Editor-in-Chief
Prof. Christopher W. Jones
Georgia Institute of Technology, USA

Open for Submissions 

pubs.acs.org/jacsau  ACS Publications
Most Trusted. Most Cited. Most Read.